Atmos. Meas. Tech. Discuss., 8, 5329–5362, 2015
www.atmos-meas-tech-discuss.net/8/5329/2015/
doi:10.5194/amtd-8-5329-2015
© Author(s) 2015. CC Attribution 3.0 License.

Atmospheric Measurement Techniques Discussions
Open Access

This discussion paper is/has been under review for the journal Atmospheric Measurement Techniques (AMT). Please refer to the corresponding final paper in AMT if available.

A new method for the absolute radiance calibration for UV/vis measurements of scattered sun light

T. Wagner[1], S. Beirle[1], S. Dörner[1], M. Penning de Vries[1], J. Remmers[1], A. Rozanov[2], and R. Shaiganfar[1]

[1]Max-Planck-Institute for Chemistry, Mainz, Germany
[2]Institute for Environmental Physics, University of Bremen, Bremen, Germany

Received: 30 March 2015 – Accepted: 6 May 2015 – Published: 28 May 2015

Correspondence to: T. Wagner (thomas.wagner@mpic.de)

Published by Copernicus Publications on behalf of the European Geosciences Union.

Abstract

Absolute radiometric calibrations are important for measurements of the atmospheric spectral radiance. Such measurements can be used to determine actinic fluxes, the properties of aerosols and clouds and the short wave energy budget. Conventional calibration methods in the laboratory are based on calibrated light sources and reflectors and are expensive, time consuming and subject to relatively large uncertainties. Also, the calibrated instruments might change during transport from the laboratory to the measurement sites. Here we present a new calibration method for UV/vis instruments that measure the spectrally resolved sky radiance, like for example zenith sky Differential Optical Absorption Spectroscopy (DOAS-) instruments or Multi-AXis (MAX-) DOAS instruments. Our method is based on the comparison of the solar zenith angle dependence of the measured zenith sky radiance with radiative transfer simulations. For the application of our method clear sky measurements during periods with almost constant aerosol optical depth are needed. The radiative transfer simulations have to take polarisation into account. We show that the calibration results are almost independent from the knowledge of the aerosol optical properties and surface albedo, which causes a rather small uncertainty of about $< 7\,\%$. For wavelengths below about 330 nm it is essential that the ozone column density during the measurements is constant and known.

1 Introduction

Measurements of the spectrally resolved sky radiance are important for many remote sensing applications in atmospheric chemistry and physics. They are also useful for the quantification of the energy yield of photovoltaic cells or doses of harmful UV radiation. Possible applications include:

– Improvement of aerosol retrievals from MAX-DOAS observations: if the measured radiances are absolutely calibrated, they don't have to be normalised by zenith sky

AMTD
8, 5329–5362, 2015

observations. This allows e.g. to better constrain the total aerosol optical depth (AOD).

- Improved quantification of the aerosol absorption: usually the sensitivity of MAX-DOAS retrievals to the aerosol single scattering albedo is rather weak. Here measurements of the absolute radiances may help to separate aerosol absorption from extinction.
- Better cloud characterisation: the brightness of clouds at the bottom or the sides depends on their optical depth, shape and internal structure. Absolute radiances measured at various angles can be quantitatively compared with results from 3-D cloud models to constrain the cloud properties.
- Extraction of well calibrated colour index values: from radiometrically calibrated spectra, colour indices can be extracted, which can be directly compared to the results from radiative transfer models.
- Estimation of actinic fluxes: from absolutely calibrated MAX-DOAS spectra taken at different elevation angles (and possibly also different azimuth angles) the spectrally resolved actinic flux over the observed wavelength range can be estimated.
- Estimation of UV doses at the surface: from absolutely calibrated MAX-DOAS measurements the UV fluxes at the surface can be estimated. Here it should, however, be noted that a constant O_3 column during the measurements is a prerequisite for an accurate radiometric calibration in the UV.
- Quantification of the radiation budget: from absolutely calibrated MAX-DOAS spectra in the UV/visible/near-IR, the amount of the downward shortwave radiation can be calculated.
- Estimation of the energy yield of photovoltaic cells. Here measurements of the angular distribution of the sky radiance are essential.

AMTD
8, 5329–5362, 2015

Absolutely calibrated measurements of the sky radiance are usually elaborate and complex, because the calibration is performed in a laboratory using e.g. calibrated light sources and reflecting surfaces. Also the errors of the radiometric calibration can be quite large: typical uncertainties of the calibration procedures for atmospheric radiance measurements are reported to range from 3 to 10 % (Pissulla et al., 2009). From comparison exercises during field campaigns even larger differences between individual instruments have been reported (up to 33 %, see Pissulla et al., 2009). Here it is interesting to note that measurements of the solar irradiance usually show much better agreement (e.g. Wuttke et al., 2006).

In this study we present a new method for the absolute radiometric calibration of instruments that observe spectrally resolved scattered sun light, which is completely independent from laboratory measurements. Instead it is based on the comparison of measurements of scattered sun light under well-defined conditions with radiative transfer simulations. In particular the dependence of the observed sky radiance on the solar zenith angle (SZA) is investigated. Continuous measurements during a couple of hours on one day are sufficient for the application of our method.

The new calibration method is particularly suitable for Differential Optical Absorption Spectroscopy (DOAS) measurements (Platt and Stutz, 2008). DOAS measurements of direct or scattered sunlight in the UV, visible and near IR spectral range are widely used to identify and quantify spectral absorption features of atmospheric trace gases. DOAS instruments are usually not radiometrically calibrated, because the DOAS technique is sensitive to differential absorption structures and does not require absolute calibration. But some of the data products derived from DOAS observations (see above) can be improved if radiometrically calibrated DOAS instruments are used. Our new method can also be applied to other measurements of scattered sun light (e.g. spectroradiometer or sun photometer measurements).

The paper is organised as follows: in Sect. 2 the data sets used in our study (MAX-DOAS measurements and radiative transfer simulations) are introduced. Section 3 presents the application of the method together with an estimation of the uncertain-

AMTD
8, 5329–5362, 2015

ties. Also the effects of (neglecting) polarisation and rotational Raman scattering are discussed. Section 4 presents the conclusions.

2 Data sets

2.1 MAX-DOAS measurements

We use MAX-DOAS observations performed during the Cabauw Intercomparison Campaign of Nitrogen Dioxide measuring Instruments (CINDI) in summer 2009 (Piters et al., 2012). They are already described in Roscoe et al. (2010) and Wagner et al. (2014), but the most important measurement properties are briefly described below: our instrument is a so called Mini-MAX-DOAS instrument covering the wavelength range from 312–458 nm with a spectral resolution between 0.45 and 0.8 nm. The typical integration time is 1 min, the field of view is $\sim 1.2^{\circ}$. During the CINDI campaign measurements with our instrument in exact zenith view (90° elevation angle) were not possible, because the instrument was operated close to at a tall tower. Thus we used measurements made in near-zenith direction at an elevation angle of 85°. The viewing azimuth direction was towards west-northwest (287° with respect to North). The measured light is dispersed by a temperature-stabilised miniature spectrometer (Ocean Optics USB2000) and recorded by a one-dimensional CCD detector (Sony ILX511). The detector signal is expressed as detector readout per time (counts per second). The optical throughput of the instrument is not known, since it depends on the efficiencies of the detector, the diffraction grating, a tilted mirror, a glass fibre and the telescope lens.

For this study, radiances are extracted from the measured spectra for discrete wavelengths ranging from 315 to 455 nm in intervals of 10 nm. The extracted radiances are calculated as averages over 7 detector pixels (~ 0.5 nm) around the selected wavelengths.

AMTD
8, 5329–5362, 2015

We applied our method to measurements made on the morning of 24 June 2009. This morning was completely cloud-free as indicated by a ground based digital camera (with images taken every 10 min) as well as by a backscatter LIDAR (see Wagner et al., 2014). The aerosol optical depth (AOD) was low and constant throughout most of the morning according to sun photometer measurements, see Fig. 1. After about 10:00 UTC the AOD increased and clouds appeared around noon (Wagner et al., 2014). In a first attempt we used all measurements between 03:00 and 09:41 UTC, representing a solar zenith angle (SZA) range between 90 and 37°. During the analysis, however, it turned out that the calibration results significantly improved if only measurements before 08:05 UTC (SZA ~ 50°) were used (see Sect. 3). This finding is probably related to the smaller variation of the AOD before ~ 08:00 UTC. In addition, the exclusion of small scattering angles might play a role. Both time periods are indicated by the black arrows in Fig. 1.

2.2 Radiative transfer simulations

Radiances are simulated with the full spherical Monte-Carlo radiative transfer model MCARTIM (Deutschmann et al., 2011). The model output can be generated in scalar or vector mode. Also the effect of rotational Raman scattering (RRS) can be considered. In most simulations we considered polarisation, but did not consider RRS (see details below). The specific parameters for Rayleigh (and rotational Raman scattering) are adapted from Landgraf et al. (2004). The parameterisation of the anisotropy of the polarisability is based on Chance and Spurr (1997). The output of the model is the normalised radiance:

$$R_{\mathrm{norm}}(\lambda) = \frac{R(\lambda)}{I(\lambda)} \tag{1}$$

Here R is the radiance (e.g. in units of $\mathrm{W\,m^{-2}\,nm^{-1}\,sr^{-1}}$) and I is the solar irradiance (e.g. in units of $\mathrm{W\,m^{-2}\,nm^{-1}}$). To obtain the radiance from the model output, the

AMTD
8, 5329–5362, 2015

normalised radiance has to be multiplied by the solar irradiance.

$$R(\lambda) = I(\lambda) \cdot R_{\text{norm}}(\lambda) \quad (2)$$

Here we use a solar irradiance spectrum from Chance and Kurucz (2010), which has an accuracy of about 1 % according to a study by Thuillier et al. (2004). Before it is applied to Eq. (2) it is multiplied by 0.969 to account for the effect of the changing sun-earth distance (during our measurement the sun-earth distance is 1.6 % larger than for the measurement of the sun irradiance spectrum). Here it is interesting to note that changes of the solar irradiance during the solar cycle are rather small. Haigh et al. (2010) studied the changes between 2004 and 2007 (which are similar to those between 2004 and 2009) and found variations < 1 % for wavelengths > 350 nm. For shorter wavelengths the uncertainties slightly increase (for 315 nm they are about 1.5 %).

In the next step the solar irradiance spectrum is convoluted with the slit function of our instrument (see Fig. 2) to make the simulation results directly comparable to the measured radiances. In addition to the convolution, averages of the simulated radiance over intervals of 0.5 nm around the selected wavelengths are calculated to exactly match the radiances of the measured spectra (see Sect. 2.1). Here, in particular the following points are important:

a. To achieve consistency between the wavelength calibrations of the measured and simulated spectra, the spectral calibration of the measured spectrum should be performed by fitting the measured spectrum against the convoluted solar irradiance spectrum.

b. The spectral convolution of the solar irradiance spectrum should be performed using a slit function which matches that of the measured spectra. We determined the slit function of our instrument by fitting the convoluted high resolution solar spectrum (step a) to the measured spectra. During the fit process the full width at half maximum (FWHM) of the Gaussian convolution kernel is varied until best

AMTD
8, 5329–5362, 2015

agreement is found. The derived FWHM ranges between about 0.80 at 315 and 0.45 at 355 nm. We used the wavelength dependent FWHM for the convolution of the high resolution solar spectrum. The temporal variation of the FWHM during the period of our measurements is < 1 %.

c. The extracted irradiance should be averaged over the same interval, as that over which the measured radiance is extracted (in this study 7 detector pixel corresponding to about 0.5 nm).

Small deviations from this procedure can lead to large errors of the simulated radiances. For example, a spectral shift of 0.2 nm can cause deviations of the extracted irradiances of up to 16 % for the wavelengths selected in this study.

Another important aspect of the radiative transfer simulations at short wavelengths (below about 330 nm) is to consider the correct ozone column density for the day of the measurements. Unfortunately, it turned out that the O_3 column density strongly changed during the period of our measurements (from about 290 to 310 DU), and strong horizontal gradients were also present (see Figs. A1 and A2 in the Appendix). Thus radiative transfer simulations using a single ozone profile (in our simulations we used a profile from the US standard atmosphere, see Fig. A2 in the Appendix) cannot well describe the radiances below 330 nm for the complete period of the measurements, and accordingly our calibration results for these wavelengths have to be interpreted with caution.

For the simulations we defined several scenarios with different atmospheric and surface properties. In addition, we performed simulations considering or not considering polarisation and rotational Raman scattering. The different scenarios are summarised in Table 1. For all scenarios radiances are simulated for AOD ranging from 0 to 0.5 (0, 0.02, 0.05, 0.1, 0.15, 0.2, 0.3, 0.4, 0.5). The viewing angle, SZA, and relative azimuth angle used in the simulations were adapted to each individual measurement. The radiances are simulated for a FOV of 1.2°.

AMTD
8, 5329–5362, 2015

2.2.1 Aerosol phase functions

We used different aerosol phase functions: for the standard scenario a Henyey–Greenstein (HG) parameterisation with an asymmetry parameter (AP) of 0.68 was used. For further scenarios we applied AP of 0.60, 0.75 and 0.85. In addition to the HG phase functions, we used scenarios with Mie-phase functions. They were calculated for log size distributions centered around 500 and 1000 nm, respectively. The width of the size distribution (SD) was assumed to 50 %. The real part of the refractive index was set to 1.34; the imaginary part was set to 0.

2.2.2 Surface albedo

The measurement site is surrounded mainly by grassland. Thus for the standard scenario a surface albedo of 0.05 was assumed. In further scenarios we also used values of 0.03, 0.07, and 0.10. To investigate the influence of the changing solar illumination on the surface reflection we performed simulations for an SZA dependent surface albedo α (SZA). For that purpose we used the parameterisation described in Briegleb et al. (1986):

$$\alpha(\mathrm{SZA}) = \alpha_0 \cdot \frac{1 + C}{1 + 2C \cdot \cos(\mathrm{SZA})} \tag{3}$$

They suggest a value of $C = 0.40$ for grasslands, while a more recent study by Wang et al. (2007) assumed a smaller value of $C = 0.26$. For our simulations we used the higher value of 0.40 to derive an upper limit of the effect of the changing solar illumination. Here it is interesting to note that the assumption of an SZA dependent albedo systematically overestimates the effect of the changing solar illumination, because in the considered wavelength range multiple scattering plays an important role. Thus most photons reaching the surface did not directly originate from the sun, but were scattered in the atmosphere. For our simulations we chose $\alpha_0 = 0.0455$ (corresponding to a surface albedo of 0.05 for SZA = 70°).

AMTD
8, 5329–5362, 2015

2.2.3 NO_2 absorption

At the measurement site rather high NO_2 concentrations occurred, which might influence the measured radiances. In addition, the effect of stratospheric NO_2 might be important. To investigate the possible effect of the atmospheric NO_2 absorption, we defined one scenario including NO_2 absorption. From the MAX-DOAS measurements we retrieved a tropospheric NO_2 VCD of about 10^{16} molecules cm^{-2} during the period of our measurements. For the stratosphere we assumed an NO_2 VCD of 3.5×10^{16} molecules cm^{-2}, based on satellite observations. The tropospheric NO_2 layer is assumed to be between the surface and 500 m; the maximum of the stratospheric NO_2 is assumed to be at an altitude of 25 km (with a full width at half maximum of 14 km).

2.2.4 Stratospheric aerosols

Compared to the aerosols in the boundary layer the optical depth of stratospheric aerosols is usually rather low (except after major volcanic eruptions). Thus we neglected stratospheric aerosols in our simulations. To estimate the potential effect of stratospheric aerosols, we defined an additional scenario including stratospheric aerosols (in a layer between 20 and 30 km altitude with an optical depth of 0.01). We used an HG phase function with AP of 0.68 and a single scattering albedo of 1.0.

2.2.5 Temperature and pressure profiles

In our simulations we used temperature and pressure profiles from the US standard atmosphere (United States Committee on Extension to the Standard Atmosphere, 1976). To estimate the influence of temperature and pressure variations, we defined an additional scenario using temperature and pressure profiles for our measurements obtained from the European Centre for Medium-Range Weather Forecasting ECMWF. For the

AMTD
8, 5329–5362, 2015

time and location of our measurement the pressure (temperature) is about 0.9 % (5 K) larger in the troposphere compared to the US standard atmosphere.

3 Radiance calibration by fitting measured and simulated radiances

In Fig. 3 the measured radiances (blue lines) are compared to simulated radiances for different AOD (ranging from 0 to 0.5). Measurements and simulation results are displayed as function of the SZA, but with separate y axes because of their different units (either in counts s^{-1} or in $W\,m^{-2}\,nm^{-1}\,sr^{-1}$). The maxima of both scales are chosen such that measurements and model results are roughly in agreement. It is obvious that not only the absolute values of the simulations, but also the curvature of the SZA dependence varies with AOD. This dependence is exploited by our method. The corresponding figures for all selected wavelengths are shown in the Appendix (Fig. A4).

The simulated radiances over the considered SZA range are fitted to the measurements by optimising a scaling factor S until a minimum of the sum of the squared differences between both data sets is reached:

$$\sum_{i=\mathrm{SZA_{min}}}^{\mathrm{SZA_{max}}} [R(\mathrm{AOD},\lambda,i) - S(\mathrm{AOD},\lambda)\cdot D(\lambda,i)]^2 \Rightarrow \min \quad (4)$$

Here $R(\mathrm{AOD},\lambda,i)$ indicate the simulated radiances at wavelength λ for a given AOD, $D(\lambda,i)$ are the values of the detector read-out at wavelength λ, and $S(\mathrm{AOD},\lambda)$ is the scaling factor. The fit is performed separately for the different scenarios, wavelengths and assumed AOD. Examples of the fit results as function of the AOD for two selected scenarios (top: HG phase function with AP = 0.75, bottom: AP = 0.60) and wavelengths are presented in Fig. 4. The RMS shows a clear minimum for a given AOD indicating that for this AOD the shape of the SZA dependence of the simulated radiances best fits the measurements. For this AOD the derived scaling factor represents the derived absolute calibration of the instrument. Interestingly, similar scaling factors are found

AMTD
8, 5329–5362, 2015

for both scenarios, although the minimum RMS is found at quite different AOD. This is a very important finding, because it indicates that our method is rather independent from the exact knowledge of the aerosol phase function.

Figure 5 gives an overview on the wavelength dependence of the derived scaling factors. The different graphs show results for different SZA ranges (the lower boundary was varied while the upper boundary was fixed to 90°). The most important conclusions from the results shown in Fig. 5 are:

a. The scaling factors are similar for the different scenarios.

b. The scaling factors are smooth functions of the wavelength.

The first finding indicates that the new calibration method is rather independent from the assumptions on the aerosol properties (and other assumed parameters, see Table 1) confirming the results presented in Fig. 4. The second finding indicates that the statistical uncertainty of the method is rather low.

Interestingly the spread of the results is largest for the largest SZA ranges. This finding first surprised us, because we expected that using more measurements should lead to more stable results. However, the larger variability of the AOD after ~ 08:00 UTC (corresponding to a SZA of 50°, see Fig. 1) is probably the main cause for the larger differences for the larger SZA interval. Another reason might be that for lower SZA the scattering angle decreases, and thus the influence of the aerosol phase function increases. The fact that those results are most dependent on phase function (Fig. 5a) also seem to point in this direction. In the following we use the SZA range from 50 to 90°.

In Fig. 6 the results for the different scenarios are compared in more detail. The upper panel of Fig. 6a shows ratios of the scaling factors for the different phase functions compared to the standard scenario. The derived scaling factors agree within about 10 %, with decreasing differences towards shorter wavelengths. Also shown are the fit results for the RMS (second panel) and the derived AOD (lower panel). While the RMS is similar for all phase functions, the AOD shows a large spread. Small AOD (similar to

AMTD
8, 5329–5362, 2015

the simultaneous AERONET results) are found for HG phase functions with small AP (0.60). The highest AOD is retrieved for the HG phase function with AP of 0.85 and for both Mie phase functions. At 315 and 325 nm the retrieved AOD shows no meaningful results because of the influence of the ozone absorption.

Figure 6b presents results for different aerosol single scattering albedos. For stronger aerosol absorption smaller scaling factors are found, but the differences are small (< 5 %). The derived RMS and AOD hardly depend on the assumed aerosol single scattering albedo.

In Fig. 6c the effect of varying the surface albedo is shown. Again very small variations of the derived scaling factors, RMS and AOD are found. Interestingly, for the scenario with the SZA dependent albedo, the largest RMS is derived. This finding might indicate that the assumed SZA dependence indeed overestimates the influence of the changing solar illumination (see Sect. 2.2.2).

Figure 6d shows results for different atmospheric parameters (see Table 1). The effects of aerosol layer height, temperature and pressure profiles, stratospheric aerosols, and NO_2 absorption have again a rather small effect on the derived scaling factors, RMS and AOD. The scenario referred to as "Cabauw" includes at the same time several changes compared to the standard scenario: temperature and pressure profiles are taken for the day of the measurements, and also stratospheric aerosols and NO_2 absorption are included. In addition, Raman scattering is considered. This scenario probably best describes the atmospheric conditions during our measurements. The effect of the combined changes of the Cabauw scenario on the scaling factors compared to the standard scenario is still small (< 5 %).

In Fig. 6e we show the effect of polarisation and rotational Raman scattering. The influence of rotational Raman scattering on the scaling factors is very small (< 2 %). The largest deviations occur – as expected – for wavelengths close to strong spectral variations of the solar irradiance (see Fig. 2). In contrast, the neglect of polarisation has a rather strong effect on the fit results: much lower scaling factors and much higher RMS and AOD compared to the standard scenario are derived.

AMTD
8, 5329–5362, 2015

Figure 7 presents an example of a calibrated radiance spectrum measured at 06:54 UTC (SZA = 61°) based on the scaling factors for the "Cabauw"-scenario. Unfortunately, we have no possibility for a direct comparison to another radiance spectrum measured at the same location and time. But in a publication by Seckmeyer et al. (2009) we found radiance spectra measured in zenith direction under similar atmospheric conditions (clear sky, SZA = 62°) in Hanover, Germany. Unfortunately, the raw data of those spectra are no more available. Thus we graphically copied a radiance spectrum (for a SZA of 62°) from the original figure in Seckmeyer et al. (2009) and overlaid it on our calibrated spectrum. Note that the measurement in Hannover was scaled by a factor of 0.97 to account for the effect of the slightly different viewing geometries (exact zenith view, compared to 85° elevation angle of our measurement). For wavelengths > 335 nm our radiance spectrum agrees very well with the radiance spectrum measured at Hannover. The discrepancies below 335 nm are probably related to the influence of the ozone absorption.

3.1 Comparison with AERONET

During the fit process not only the scaling factor for the absolute calibration is determined, but also the AOD (see Figs. 4 and 6). The choice of the aerosol phase function has the strongest effect on the retrieved AOD, while other parameters (see Table 1) have only a small influence. Very good agreement with AERONET AOD is found for the scenario with an aerosol asymmetry parameter of 0.60. Large deviations are found for HG phase functions with AP of 0.85 and both Mie phase functions. Also the neglect of polarisation leads to unrealistically high AOD.

The comparison to the AERONET results is very useful, because it allows an independent assessment of the results of the new method. Furthermore, based on the comparison to the AERONET AOD, the uncertainties of the new calibration method (see Fig. 4) can be further reduced, because scenarios with unrealistic AOD results can be simply disregarded. Here it should be noted that the retrieved AOD for wavelengths < 330 nm are not meaningful for our measurements because of the strong

AMTD
8, 5329–5362, 2015

change of the ozone layer during the measurements (see Figs. A1 and A2 in the Appendix). Disregarding the scenarios with the largest deviations of the AOD from the AERONET measurements, from the sensitivity analyses presented in Fig. 6 we estimate the uncertainty of our calibration method to be < 6 %.

4 Conclusions

We presented a new method for the calibration of UV/vis instruments that measure the spectrally resolved sky radiance, like for example zenith sky DOAS instruments or MAX-DOAS instruments. Our method does not rely on laboratory measurements, but is based on the comparison of the solar zenith angle dependence of the measured zenith sky radiance with results from radiative transfer simulations. The prerequisites for the application of our method is that the sky is clear and the aerosol optical depth is constant and low for a period of a few hours. For observations at short wavelengths, also the thickness of the ozone layer should be constant (and known) during the measurements. We selected measurements during a period of about 4 h covering a SZA range between 50 and 90°.

Apart from being a simple and cheap procedure, another advantage of our method is that the calibration is derived directly from the atmospheric spectra, thus excluding the occurrence of potential changes of the instrument during the transport from the laboratory to the field. The radiometric calibration can be determined for individual wavelengths; in this study we selected wavelengths in intervals of 10 nm between 315 and 455 nm (the wavelength range of our instrument). The calibration function was found to be spectrally smooth and can therefore be interpolated (if the intervals are not chosen too large). Alternatively, also additional wavelengths in between the chosen wavelengths could be used.

From our method also the aerosol optical depth for the selected wavelengths is determined. The comparison of the derived AOD with AOD derived from AERONET observations can be used to assess the quality of the calibration results. In particular, sce-

AMTD
8, 5329–5362, 2015

narios yielding unrealistic AOD values can be removed. If we do not take into account scenarios, which yield unrealistically high AOD, the variation of the derived calibration results is further reduced. From the sensitivity studies based on different scenarios, we estimate the uncertainty of our method to be < 7 % (including the uncertainties of the solar irradiance measurement). Here it should be noted that for larger AOD probably larger uncertainties have to be expected. This aspect should be investigated in future studies.

Our results clearly indicate that the radiative transfer simulations have to consider polarisation. In contrast, the effect of rotational Raman scattering can be neglected.

Our new method is of importance to many applications including the determination of actinic fluxes, the characterisation of aerosol and cloud properties or the quantification of the short wave radiative flux at the position of the instrument. Another interesting application might be the quantification of the yield of photovoltaic cells.

Appendix

For our simulations we used an ozone profile from the US standard atmosphere (United States Committee on Extension to the Standard Atmosphere, 1976) with an O_3 VCD of 345 DU (see Fig. A1). Later it turned out that two measured ozone profiles close to the measurements site were available from SCIAMACHY limb observations (Sonkaew et al., 2009). These profiles showed smaller O_3 VCDs: 296 and 331 DU (Fig. A1). The rather large difference between the two neighbouring O_3 profiles indicates strong horizontal gradients close to Cabauw on that day. These gradients are also indicated by the strong temporal variation of the O_3 VCD (see Fig. A2).

The radiances simulated for the different O_3 profiles are shown in Fig. A3. The largest differences are found at short wavelengths and for small SZA. For these SZA the variation of the O_3 VCD has a strong impact on the radiances, while the influence of the profile shape is relatively small. In contrast, for SZA close to 90° the relative profile shape has a strong effect on the relative difference of the simulated radiances (Umkehr

AMTD
8, 5329–5362, 2015

effect, see Götz et al., 1934). This is, however, not important for our study, because our calibration method is sensitive to the absolute differences between the measured and simulated radiances (see Sect. 3). Because of the strong temporal variation and the large spatial gradients of the O_3 VCD on the day of our measurements we did not update our simulation results with one of the measured SCIAMACHY profiles. We do not expect much improvement to the results in the presence of such strong gradients, even if a more appropriate profile (e.g. from SCIAMACHY) would be used.

Acknowledgements. We want to thank the organisers of the Cabauw Intercomparison Campaign of Nitrogen Dioxide measuring Instruments (CINDI) campaign in Summer 2009 (http://www.knmi.nl/samenw/cindi/), especially Ankie Piters and Marc Kroon. We thank J. S. (Bas) Henzing and his staff for his effort in establishing and maintaining the Cabauw AERONET site used in this investigation. The radiance measurements at Hannover (Fig. 6) were copied from a publication by Seckmeyer et al. (2009). We used the Monte Carlo radiative transfer model MCARTIM, which was developed by Tim Deutschmann.

The article processing charges for this open-access publication
were covered by the Max Planck Society.

References

Briegleb, B. P., Minnis, P., Ramanathan, V., and Harrison, E.: Comparison of regional clear sky albedos inferred from satellite observations and model calculations, J. Clim. Appl. Meteorol., 25, 214–226, 1986.

Deutschmann, T., Beirle, S., Frieß, U., Grzegorski, M., Kern, C., Kritten, L., Platt, U., Pukite, J., Wagner, T., Werner, B., and Pfeilsticker, K.: The Monte Carlo Atmospheric Radiative Transfer Model McArtim: introduction and validation of Jacobians and 3-D features, J. Quant. Spectr. Rad. Transf., 112, 1119–1137, doi:10.1016/j.jqsrt.2010.12.009, 2011.

Chance, K. and Kurucz, R. L.: An improved high-resolution solar reference spectrum for Earth's atmosphere measurements in the ultraviolet, visible, and near infrared, J. Quant. Spectrosc. Ra., 111, 1289–1295, 2010.

AMTD
8, 5329–5362, 2015

Chance, K. and Spurr R. J. D.: Ring effect studies: Rayleigh scattering, including molecular parameters for rotational Raman scattering, and the Fraunhofer spectrum, Appl. Optics, 36, 5224–5230, 1997.

Götz, F. W. P., Meetham, A. R., and Dobson, G. M. B.: The vertical distribution of ozone in the atmosphere, P. Roy. Soc. Lond. A Mat., 145, 416–446, 1934.

Haigh, J. D., Winning, A. R., Toumi, R., and Harder, J. W.: An influence of solar spectral variations on radiative forcing of climate, Nature, 467, 696–699, doi:10.1038/nature09426, 2010.

Hönninger G. and Platt, U.: Observations of BrO and its vertical distribution during surface ozone depletion at Alert, Atmos. Environ., 36, 2481–2490, 2002.

Landgraf, J., Hasekamp, O. P., van Deelen, R., and Aben, I.: Rotational Raman scattering of polarized light in the Earth atmosphere: a vector radiative transfer model using the radiative transfer perturbation theory approach, J. Quant. Spectrosc. Ra., 87, 399–433, 2004.

Mishchenko, M. I., Lacis, A. A., and Travis, L. D.: Errors induced by the neglect of polarisation in radiance calculations for Rayleigh-scattering atmospheres, J. Quant. Spectrosc. Ra., 51, 3, 491–510, 1994.

Piters, A. J. M., Boersma, K. F., Kroon, M., Hains, J. C., Van Roozendael, M., Wittrock, F., Abuhassan, N., Adams, C., Akrami, M., Allaart, M. A. F., Apituley, A., Beirle, S., Bergwerff, J. B., Berkhout, A. J. C., Brunner, D., Cede, A., Chong, J., Clémer, K., Fayt, C., Frieß, U., Gast, L. F. L., Gil-Ojeda, M., Goutail, F., Graves, R., Griesfeller, A., Großmann, K., Hemerijckx, G., Hendrick, F., Henzing, B., Herman, J., Hermans, C., Hoexum, M., van der Hoff, G. R., Irie, H., Johnston, P. V., Kanaya, Y., Kim, Y. J., Klein Baltink, H., Kreher, K., de Leeuw, G., Leigh, R., Merlaud, A., Moerman, M. M., Monks, P. S., Mount, G. H., Navarro-Comas, M., Oetjen, H., Pazmino, A., Perez-Camacho, M., Peters, E., du Piesanie, A., Pinardi, G., Puentedura, O., Richter, A., Roscoe, H. K., Schönhardt, A., Schwarzenbach, B., Shaiganfar, R., Sluis, W., Spinei, E., Stolk, A. P., Strong, K., Swart, D. P. J., Takashima, H., Vlemmix, T., Vrekoussis, M., Wagner, T., Whyte, C., Wilson, K. M., Yela, M., Yilmaz, S., Zieger, P., and Zhou, Y.: The Cabauw Intercomparison campaign for Nitrogen Dioxide measuring Instruments (CINDI): design, execution, and early results, Atmos. Meas. Tech., 5, 457–485, doi:10.5194/amt-5-457-2012, 2012.

Pissulla, D., Seckmeyer, G., Cordero, R. R., Blumthaler, M., Schallhart, B., Webb, A., Kift, R., Smedley, A., Bais, A. F., Kouremeti, N., Cede, A., Hermang, J., and Kowalewskig, M.: Comparison of atmospheric spectral radiance measurements from five independently calibrated systems, Photochem. Photobio. S., 8, 516–527, 2009.

AMTD
8, 5329–5362, 2015

Platt, U. and Stutz, J.: Differential Optical Absorption Spectroscopy, Principles and Applications, Springer, Berlin, 2008.

Roscoe, H. K., Johnston, P. V., Van Roozendael, M., Richter, A., Sarkissian, A., Roscoe, J., Preston, K. E., Lambert, J-C., Hermans, C., DeCuyper, W., Dzienus, S., Winterrath, T., Burrows, J., Goutail, F., Pommereau, J-P., D'Almeida, E., Hottier, J., Coureul, C., Didier, R., Pundt, I., Bartlett, L. M., McElroy, C. T., Kerr, J. E., Elokhov, A., Giovanelli, G., Ravegnani, F., Premuda, M., Kostadinov, I., Erle, F., Wagner, T., Pfeilsticker, K., Kenntner, M., Marquard, L. C., Gil, M., Puentedura, O., Yela, M., Arlander, D. W., Kastad Hoiskar, B. A., Tellefsen, C. W., Karlsen Tornkvist, K., Heese, B., Jones, R. L., Aliwell, S. R., and Freshwater, R. A.: Slant column measurements of O_3 and NO_2 during the NDSC intercomparison of zenith-sky UV-visible spectrometers in June 1996, J. Atmos. Chem., 32, 281–314, 1999.

Roscoe, H. K., Van Roozendael, M., Fayt, C., du Piesanie, A., Abuhassan, N., Adams, C., Akrami, M., Cede, A., Chong, J., Clémer, K., Friess, U., Gil Ojeda, M., Goutail, F., Graves, R., Griesfeller, A., Grossmann, K., Hemerijckx, G., Hendrick, F., Herman, J., Hermans, C., Irie, H., Johnston, P. V., Kanaya, Y., Kreher, K., Leigh, R., Merlaud, A., Mount, G. H., Navarro, M., Oetjen, H., Pazmino, A., Perez-Camacho, M., Peters, E., Pinardi, G., Puentedura, O., Richter, A., Schönhardt, A., Shaiganfar, R., Spinei, E., Strong, K., Takashima, H., Vlemmix, T., Vrekoussis, M., Wagner, T., Wittrock, F., Yela, M., Yilmaz, S., Boersma, F., Hains, J., Kroon, M., Piters, A., and Kim, Y. J.: Intercomparison of slant column measurements of NO_2 and O_4 by MAX-DOAS and zenith-sky UV and visible spectrometers, Atmos. Meas. Tech., 3, 1629–1646, doi:10.5194/amt-3-1629-2010, 2010.

Seckmeyer, G., Smolskaia, I., Pissulla, D., Bais, A. F., Tourpali, K., Meleti, C., and Zerefos, C.: Solar UV: measurements and trends, in: Twenty Years of Ozone Decline, Proceedings of the Symposium for the 20th Anniversary of the Montreal Protocol, Athens, 23–26 September 2007, edited by: Zerefos, C., Contopoulos, G. and Skalkeas, G., Part VI, Springer, the Netherlands, 359–368, 2009.

Sonkaew, T., Rozanov, V. V., von Savigny, C., Rozanov, A., Bovensmann, H., and Burrows, J. P.: Cloud sensitivity studies for stratospheric and lower mesospheric ozone profile retrievals from measurements of limb-scattered solar radiation, Atmos. Meas. Tech., 2, 653–678, doi:10.5194/amt-2-653-2009, 2009.

Thuillier, G., Floyd, L., Woods, T. N., Cebula, R., Hilsenrath, E., Herse, M., and Labs, D.: Solar irradiance reference spectra. in: Solar Variability and its Effect on the Earth's Atmosphere and Climate System, edited by: Pap, J. M., AGU, Washington, DC, 171–194, 2004.

AMTD
8, 5329–5362, 2015

United States Committee on Extension to the Standard Atmosphere: US Standard Atmosphere, 1976, National Oceanic and Atmospheric Administration, National Aeronautics and Space Administration, United States Air Force, Washington DC, 1976.

Wagner, T., Apituley, A., Beirle, S., Dörner, S., Friess, U., Remmers, J., and Shaiganfar, R.: Cloud detection and classification based on MAX-DOAS observations, Atmos. Meas. Tech., 7, 1289–1320, doi:10.5194/amt-7-1289-2014, 2014.

Wang, Z., Zeng, X., and Barlage, M.: Moderate resolution imaging spectroradiometer bidirectional reflectance distribution function–based albedo parameterization for weather and climate models, J. Geophys. Res., 112, D02103, doi:10.1029/2005JD006736, 2007.

Wuttke, S., Seckmeyer, G., Bernhard, G., Ehramjian, J., McKenzie, R., Johnston, P., and O'Neil, M.: New spectroradiometers complying with the NDSC standards, J. Atmos. Ocean. Tech., 23, 241–251, 2006.

AMTD
8, 5329–5362, 2015

Table 1. Overview on the different scenarios (for detailed description see Sect. 2.2). For all scenarios radiances are simulated for AOD between 0 and 0.5.

Scenario	Description
Standard (std)	Standard scenario: aerosol properties: HG phase function with asymmetry parameter of 0.68, layer: 0–1 km, single scattering albedo: 0.95, surface albedo: 0.05, temperature, pressure and O_3 profiles from the US standard atmosphere, polarisation but no Raman scattering is taken into account.
Scenario	**Deviation from standard scenario**
AP 0.60	HG phase function with asymmetry paramater of 0.60
AP 0.75	HG phase function with asymmetry paramater of 0.75
AP 0.85	HG phase function with asymmetry paramater of 0.85
Mie 500	Mie phase function for size distribution with maximum at 500 nm and SD of ±50 %, real refractive index: 1.34
Mie 1000	Mie phase function for size distribution with maximum at 1000 nm and SD of ±50 %, real refractive index: 1.34
SSA 0.90	single scattering albedo: 0.90
SSA 1.00	single scattering albedo: 1.00
0–2 km	aerosol layer height: 2 km
Albedo 0.03	surface albedo: 0.03
Albedo 0.07	surface albedo: 0.07
Albedo 0.10	surface albedo: 0.10
Albedo SZA dep.	SZA dependent surface albedo (see text)
Ring	including Raman scattering
NO_2	including NO_2 absorption (see text)
strat. aerosols	including stratospheric aerosols (see text)
T and *p*	using temperature and pressure profiles for Cabauw
Cabauw	including Raman scattering, NO_2 absorption, stratospheric aerosols and using temperature and pressure profiles for Cabauw

AMTD
8, 5329–5362, 2015

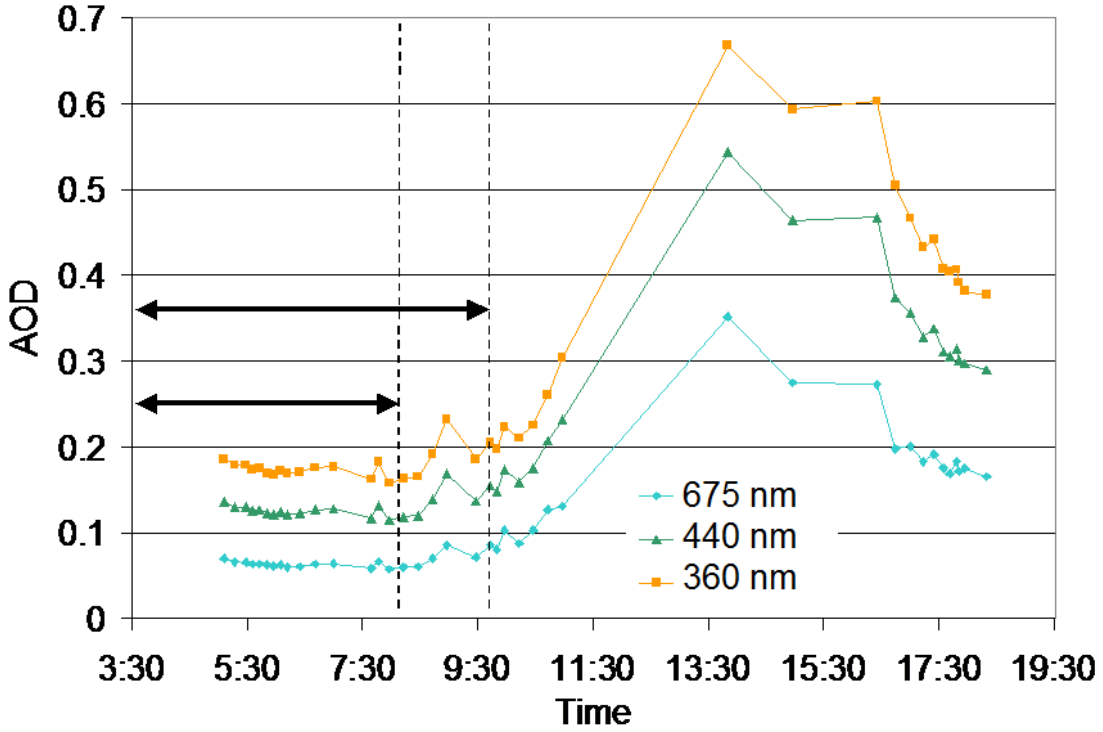

Figure 1. AOD derived from sun photometer observations (AERONET) at Cabauw at three wavelengths. The black vertical lines indicate the ends of the two measurement periods used in this study: 03:30–08:05 UTC (SZA: 90–50°); 03:30–09:41 UTC (SZA: 90–36.7°). The AERONET measurements start at 05:06 UTC (SZA: 79°).

AMTD
8, 5329–5362, 2015

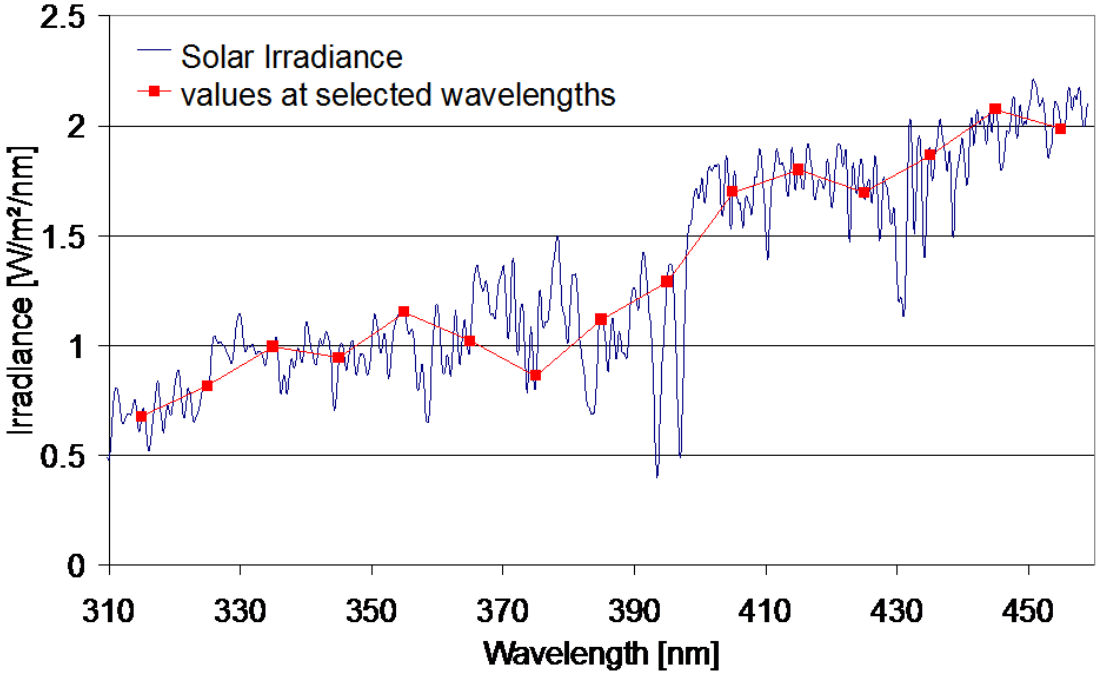

Figure 2. Convoluted solar irradiance spectrum (blue line) and extracted radiances at the specific wavelengths selected in this study.

AMTD
8, 5329–5362, 2015

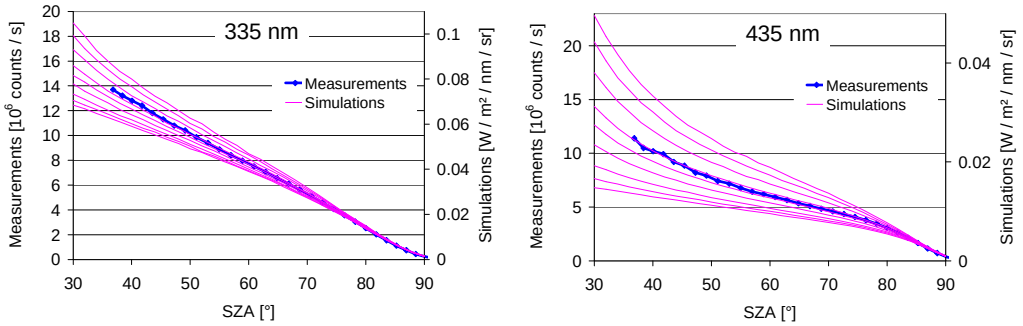

Figure 3. Comparison of measured radiances (blue, right axis) with simulated radiances (magenta lines, left axis) for two wavelengths. The lowest simulated radiances are obtained for AOD = 0; the highest radiances for AOD = 0.5. Results for additional wavelengths are shown in Fig. A4 in the Appendix.

AMTD
8, 5329–5362, 2015

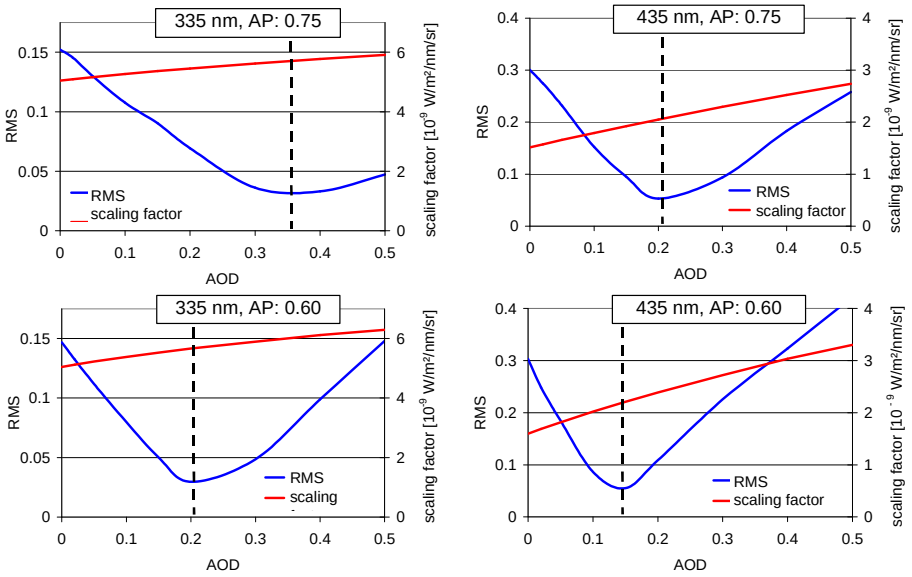

Figure 4. Scaling factors and RMS derived during the fitting process (Eq. 4) as function of the AOD for two selected scenarios and wavelengths. The scaling factor is displayed in red (right axis), the RMS in blue (left axis). In the upper panel an asymmetry parameter of 0.75 and in the lower panel one of 0.60 is used in the simulations. For both aerosol optical properties the minimum RMS of the fit is found for different AOD, but the corresponding scaling factors are almost the same.

AMTD
8, 5329–5362, 2015

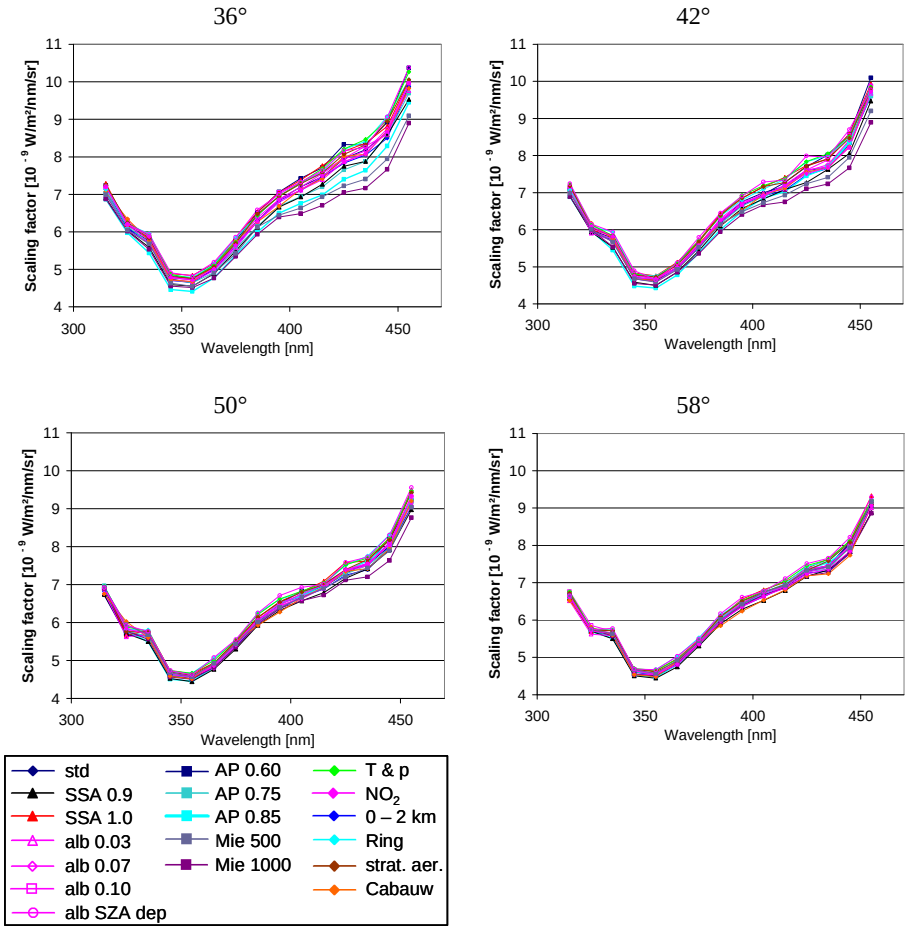

Figure 5. Derived scaling factors for different SZA intervals: the lower boundary of the SZA range is varied, while the upper boundary is always 90°. The different lines indicate the results for different scenarios (see Table 1).

AMTD
8, 5329–5362, 2015

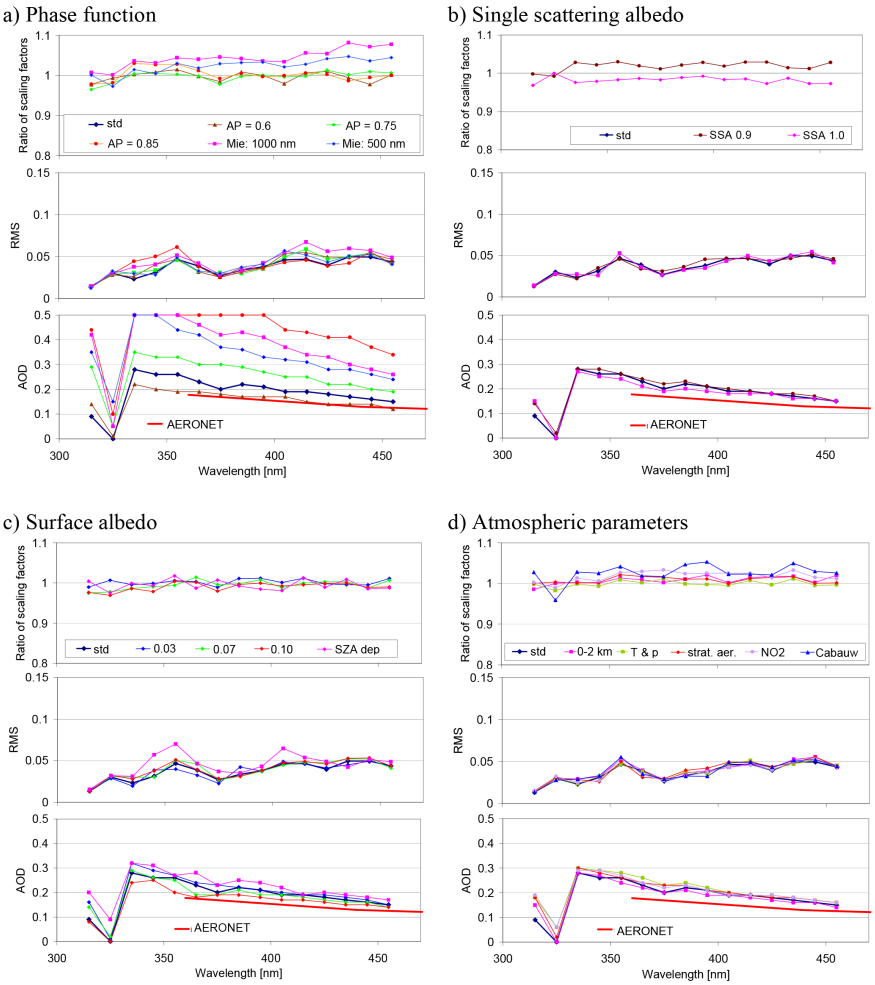

Figure 6.

AMTD
8, 5329–5362, 2015

New UV/vis radiance calibration for observations of scattered sun light

T. Wagner et al.

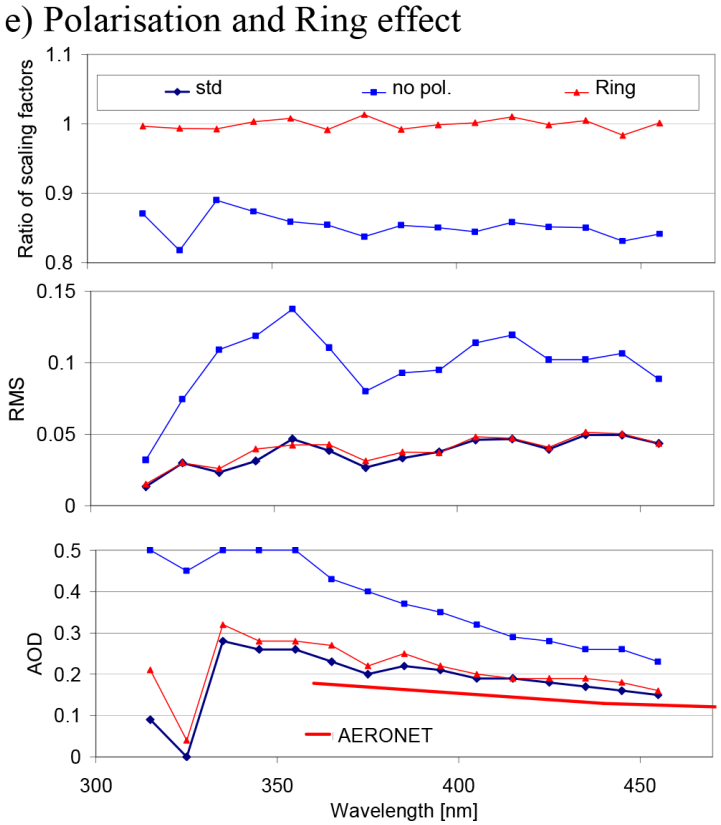

Figure 6. Comparison of the derived scaling factors, RMS and AOD for different scenarios (the scaling factors are divided by the scaling factors for the standard scenario, see Table 1).

AMTD
8, 5329–5362, 2015

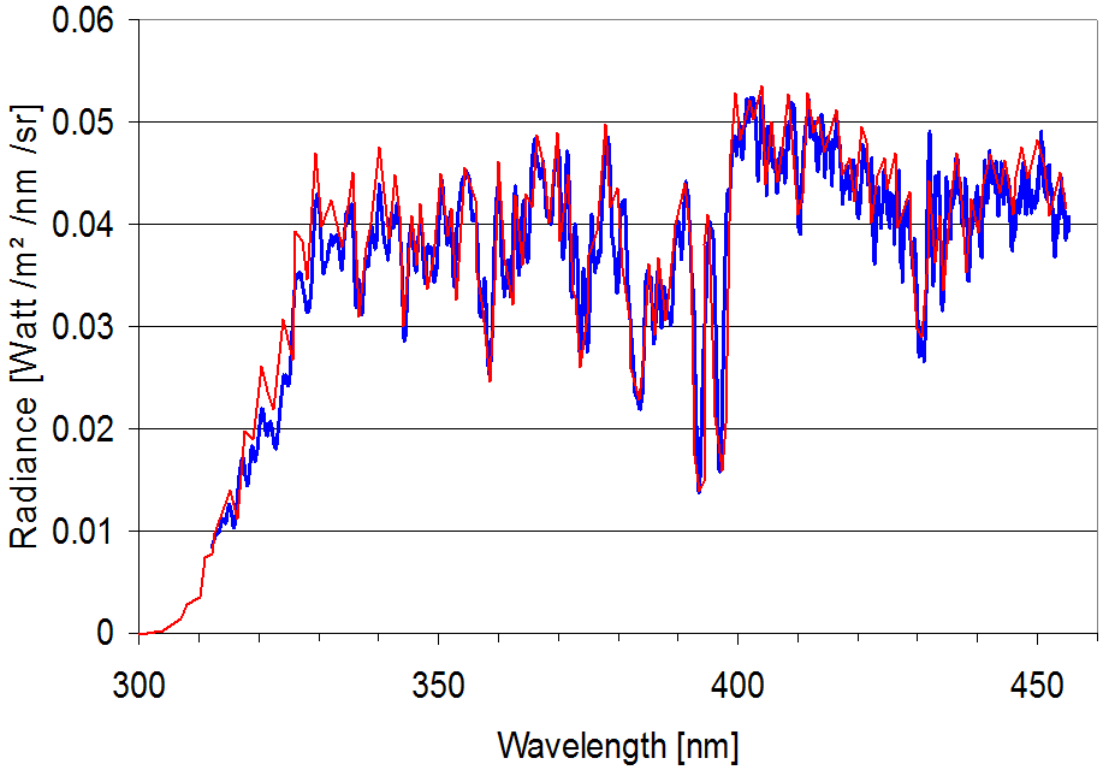

Figure 7. Comparison of a calibrated spectrum (blue), measured on 24 June 2009, 06:54 UTC, at a SZA of 61° and an independent measurement under similar conditions (red) in Hannover, Germany (clear sky, SZA: 62°, Seckmeyer et al., 2009). The measurement in Hannover was scaled by a factor of 0.97 to account for the effect of the slightly different viewing geometries (exact zenith view, compared to 85° elevation angle of our measurement).

AMTD
8, 5329–5362, 2015

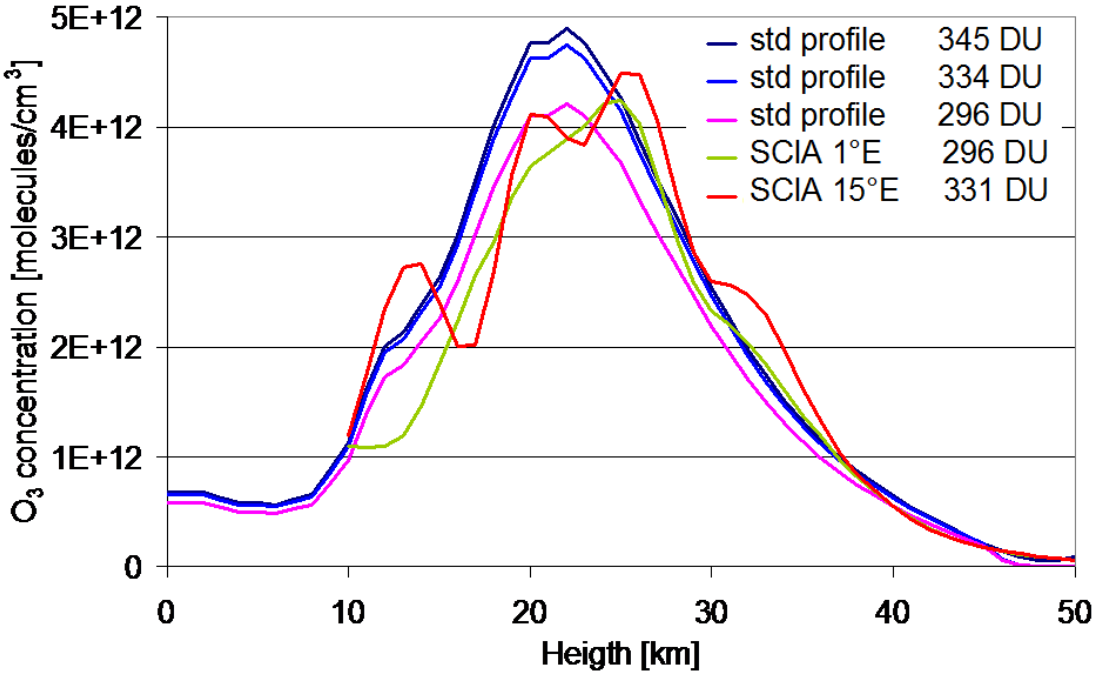

Figure A1. Comparison of different ozone profiles for the day of our measurements. The standard profile used in our simulations (345 DU) is shown together with two measured profiles from SCIAMACHY (55.62° N, 1.00° E: 296 DU; 53.89° N, 15.26° E: 331 DU). In addition, two scaled standard profiles matching the same O_3 VCD as the SCIAMACHY profiles are shown.

AMTD
8, 5329–5362, 2015

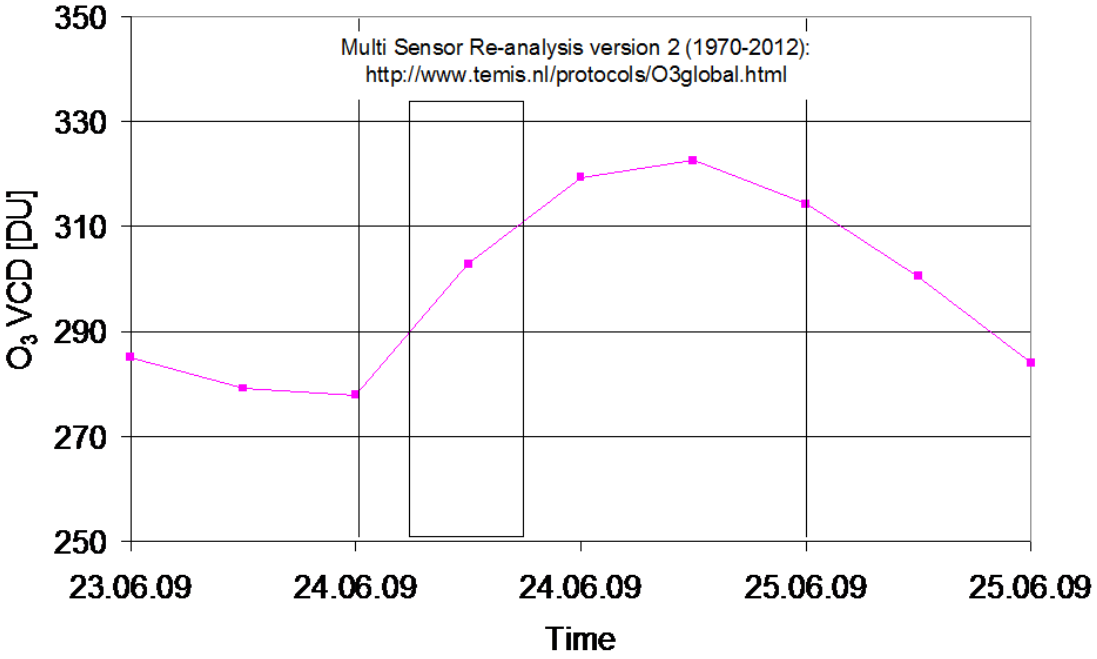

Figure A2. Time series of the O_3 vertical column density (VCD) above Cabauw during the period of our measurements (indicated by the black rectangles).

AMTD
8, 5329–5362, 2015

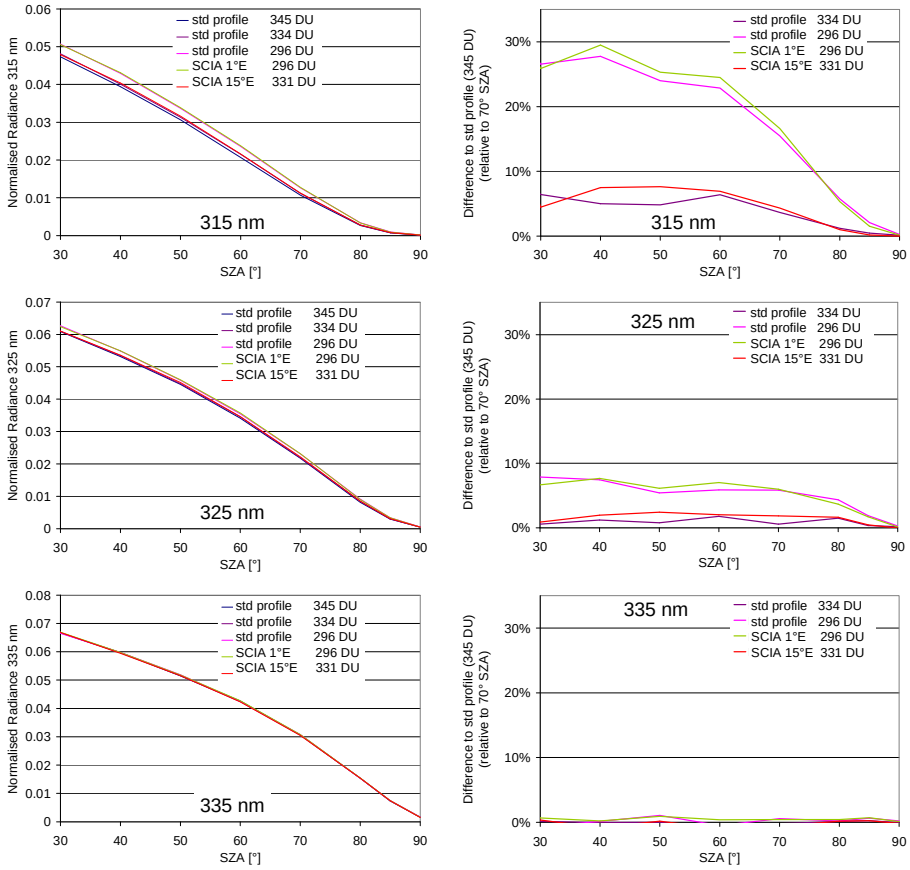

Figure A3. Left: simulated radiances for the different O_3 profiles shown in Fig. A1. The profiles differ in shape and O_3 VCD. Right: differences of the radiances compared to the standard profile (345 DU). To simplify the comparison, the differences are divided by the radiances at SZA = 70°.

AMTD
8, 5329–5362, 2015

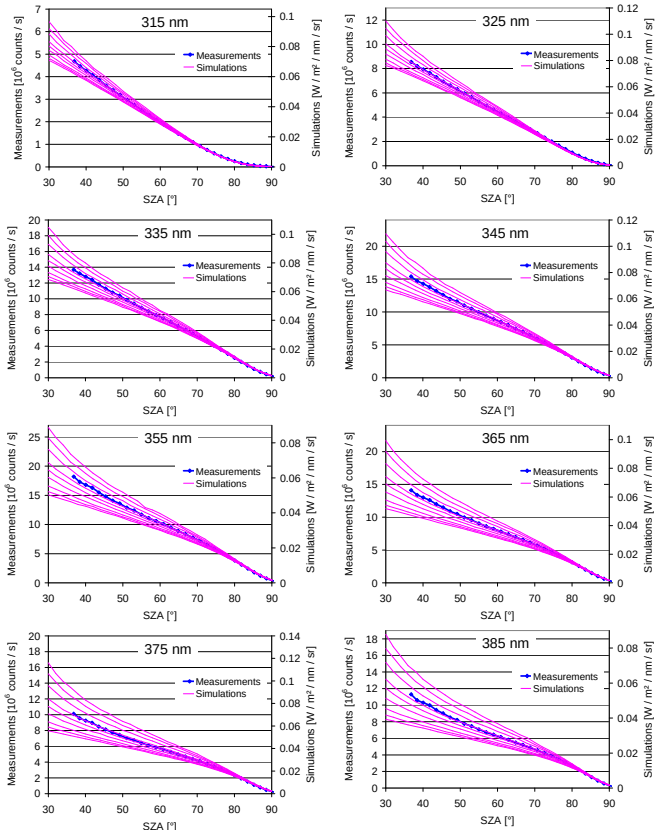

Figure A4.

AMTD
8, 5329–5362, 2015

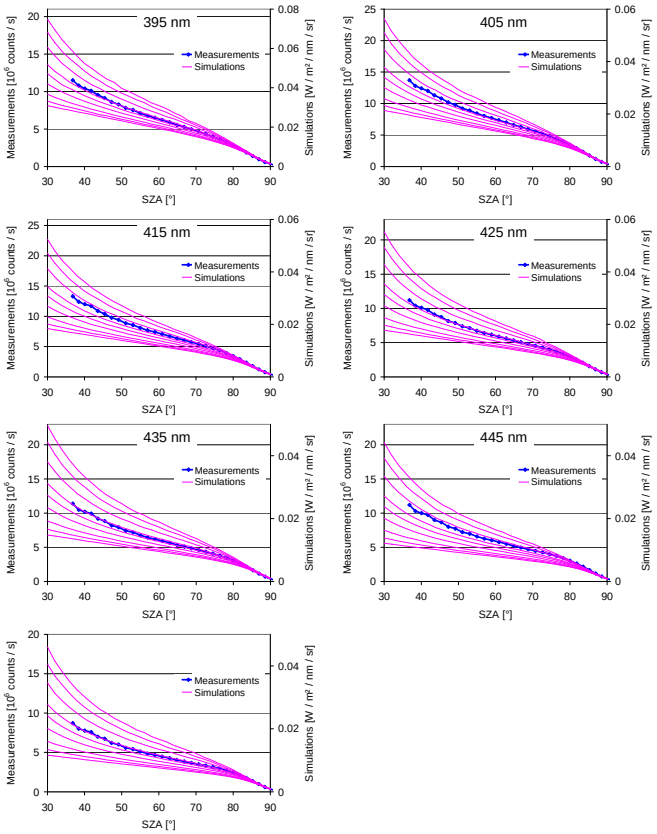

Figure A4. Comparison of measured radiances (blue, right axis) with simulated radiances (magenta lines, left axis) for all wavelengths used in our study. The lowest simulated radiances are obtained for AOD = 0; the highest radiances for AOD = 0.5.

AMTD
8, 5329–5362, 2015